# Measuring distances between TRPV1 and the plasma membrane using a noncanonical amino acid and transition metal ion FRET

William N. Zagotta, Moshe T. Gordon, Eric N. Senning, Mika A. Munari, and Sharona E. Gordon

Department of Physiology and Biophysics, University of Washington, Seattle, WA 98195

Despite recent advances, the structure and dynamics of membrane proteins in cell membranes remain elusive. We implemented transition metal ion fluorescence resonance energy transfer (tmFRET) to measure distances between sites on the N-terminal ankyrin repeat domains (ARDs) of the pain-transducing ion channel TRPV1 and the intracellular surface of the plasma membrane. To preserve the native context, we used unroofed cells, and to specifically label sites in TRPV1, we incorporated a fluorescent, noncanonical amino acid, L-ANAP. A metal chelating lipid was used to decorate the plasma membrane with high-density/high-affinity metal-binding sites. The fluorescence resonance energy transfer (FRET) efficiencies between L-ANAP in TRPV1 and $Co^{2+}$ bound to the plasma membrane were consistent with the arrangement of the ARDs in recent cryoelectron microscopy structures of TRPV1. No change in tmFRET was observed with the TRPV1 agonist capsaicin. These results demonstrate the power of tmFRET for measuring structure and rearrangements of membrane proteins relative to the cell membrane.

The Journal of General Physiology

## INTRODUCTION

The pain-transducing ion channel TRPV1 is activated by capsaicin (the pungent extract from hot chili peppers; Caterina et al., 1997), noxious heat (Caterina et al., 1997), extracellular $H^+$ (Tominaga et al., 1998) and $Mg^{2+}$ ions (Cao et al., 2014; Yang et al., 2014), anandamide (Zygmunt et al., 1999; Smart et al., 2000), lysophosphatidic acid (Nieto-Posadas et al., 2012), and phosphoinositides (Stein et al., 2006; Lukacs et al., 2007). TRPV1 has been shown to underlie thermal and chemical hyperalgesia, the phenomenon in which inflammation and injury increase the sensitivity of sensory neurons to noxious heat and chemical stimuli (Caterina et al., 2000). Given its important role in acute and chronic pain, TRPV1 is an attractive target for drug discovery (Szolcsányi and Pintér, 2013).

Like many other members of the voltage-gated superfamily of ion channels, TRPV1 channels assemble as tetramers of identical subunits, with intracellular N and C termini. The N terminus, which constitutes about half of the primary sequence, includes six ankyrin repeats that assemble into an ankyrin repeat domain (ARD; Lishko et al., 2007). Mutations and posttranslational modifications within the ARDs indicate that they can have a profound effect on the gating energetics of TRPV1 (Lishko et al., 2007; Myers et al., 2008; Salazar et al., 2008; Yao et al., 2011), suggesting that they undergo a conformational rearrangement associated with opening of the ion-conducting pore. Recently, structures of TRPV1 in amphipols were determined with cryoelectron microscopy (cryoEM) in the apo state and bound to regulators (Fig. 1 A; Cao et al., 2013; Liao et al., 2013). Comparing the structures in the apo state (presumably closed) and the capsaicin-bound state (presumably open; Cao et al., 2013) reveals hardly any conformational rearrangements either within or between ARDs. Furthermore, comparing the structure of the apo state to the structure of TRPV1 bound to both an agonist (resiniferatoxin) and an activating toxin (double-knot toxin), reveals small rigid body movements of the ARDs of the four subunits relative to one another, but little movement relative to the membrane.

In contrast to the ARDs of TRPV1, which splay away from the transmembrane core like the blades of a propeller (Fig. 1 A), the ARDs of the related TRPA1 ion channel are arranged perpendicular to the bilayer, organized by a central coiled-coil domain composed of regions of sequence in the C terminus of the channel (Fig. 1 B; Paulsen et al., 2015). Given the conservation of function—cysteine modification within the ARDs of both TRPV1 and TRPA1 leads to agonist-independent activation—the difference in structure is striking. Indeed, comparing the TRPV1 and TRPA1 structures (Fig. 1 A compared with Fig. 1 B) raises the question of whether the arrangement of the ARDs of TRPV1 in the cryoEM structure determined in amphipols faithfully

Correspondence to Sharona E. Gordon: seg@uw.edu; or William N. Zagotta: zagotta@uw.edu

Abbreviations used in this paper: ARD, ankyrin repeat domain; cryoEM, cryoelectron microscopy; FRET, fluorescence resonance energy transfer; HBSS, HEPES-buffered saline solution; TIRF, total internal reflection fluorescence; tmFRET, transition metal ion fluorescence resonance energy transfer.



The Rockefeller University Press $30.00
J. Gen. Physiol. Vol. 147 No. 2 201–216
www.jgp.org/cgi/doi/10.1085/jgp.201511531

reflects the structure of full-length channels in their native cellular environment. Methods that could measure the distance of amino acids within the ankyrin repeats relative to the plasma membrane of cells in full-length, intact channels would therefore be useful.

Here, we developed an approach for specific labeling of amino acids within TRPV1 expected to be at various distances relative to the intracellular surface of the plasma membrane and for measuring the distances between those labels and $Co^{2+}$ bound to the intracellular surface of the plasma membrane. Using amber codon suppression, we incorporated a small, fluorescent amino acid into three different positions on the ARDs of TRPV1. We show that TRPV1 channels incorporating the fluorescent amino acid are full length and functional, forming $Ca^{2+}$-permeable channels that are activated by capsaicin. Using transition metal ion fluorescence resonance energy transfer (tmFRET), we demonstrate that the distance between the fluorescent amino acids and $Co^{2+}$ bound to the intracellular surface of the plasma membrane changes with position of the fluorophore but not with the addition of capsaicin, consistent with the cryoEM structures of TRPV1. Our data support the overall arrangement of the ARDs relative to the plasma membrane seen in the cryoEM structure of TRPV1 and show that tmFRET with the membrane offers a promising new approach for measuring structure and rearrangements of membrane proteins relative to the native cell membrane.

## MATERIALS AND METHODS

### Plasmid information

pANAP (Addgene) and pEGFP were gifts from P. Schultz (The Scripps Research Institute, La Jolla, CA; Chatterjee et al., 2013), and rat TRPV1 was a gift from D. Julius (University of California, San Francisco, San Francisco, CA). For all TRPV1-TAG constructs, the TAG amber stop codon was introduced by two-step PCR using overlapping primers containing the mutation and subcloned into our previously described TRPV1-eYFP.pcDNA3 vector (Ufret-Vincenty et al., 2015). All constructs were confirmed with automated DNA sequencing.

### Cell culture and transfection

HEK 293T/17 cells (ATCC CRL-11268) were cultured at 37°C, 5% $CO_2$, in Dulbecco's modified Eagle medium (Gibco) containing 25 mM glucose, 1 mM sodium pyruvate, and 4 mM L-glutamine. Culture medium was supplemented with 10% FBS and penicillin/streptomycin. The cells were plated on 6-well trays (Corning) 1 d before transfection at a density chosen to achieve a confluency of 20–25% at the time of transfection. Cells were transfected using Lipofectamine 2000 (Gibco) according to the manufacturer's instruction with some modifications: for each well, a total of 1.6 µg DNA and 10 µl Lipofectamine in 300 µl Opti-MEM (Gibco) was used (Ufret-Vincenty et al., 2015). After 4–6 h of incubation, transfection medium was replaced by complete medium. L-ANAP-ME (AsisChem) stock was made in ethanol and was added to the medium at a final concentration of 20 µM. For all transfections with TRPV1-TAG constructs and pANAP, plasmids were used in a 3:1 ratio. For negative controls, pANAP was replaced by pcDNA3.1(−) (Invitrogen). All L-ANAP-ME–containing culture plates were protected from light during incubation by wrapping them loosely in aluminum foil.

For unroofing experiments, coverslips were prepared by incubation with filter sterilized 0.12 mg/ml polylysine (Sigma-Aldrich)

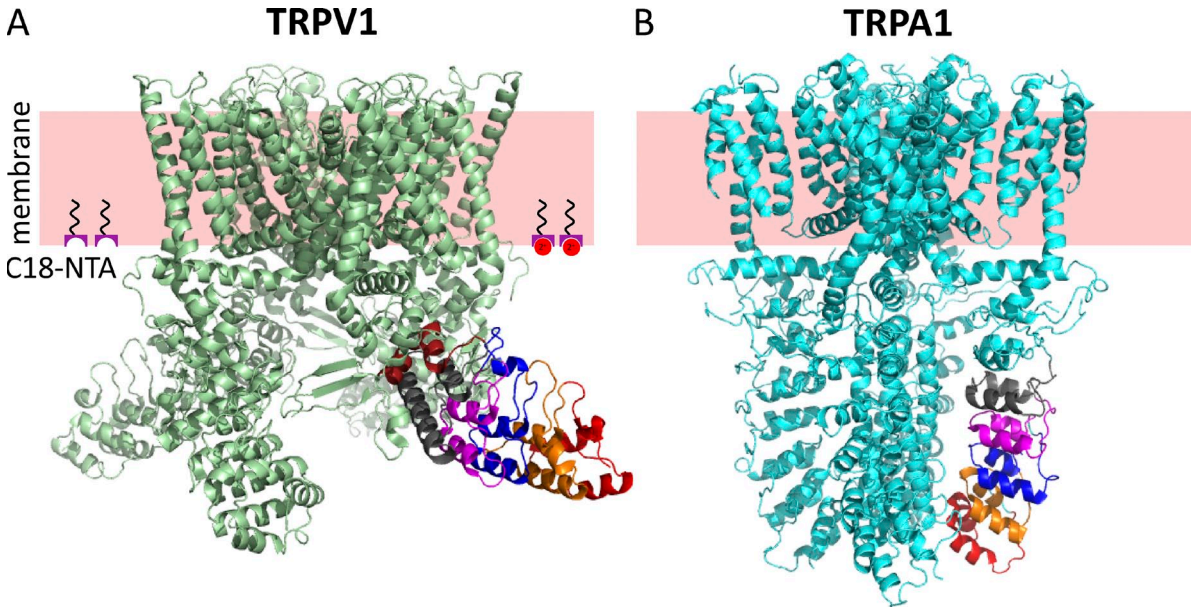


**Figure 1.** Structural divergence in ankyrin repeat domains of TRPV1 and TRPA1. (A) Structure of TRPV1 (3J5P) with ankyrin repeats 1–6 labeled in red, orange, blue, magenta, gray, and brown. The pink slab represents the approximate location of the plasma membrane, and the moieties at the intracellular surface represent C18-NTA partitioned into the membrane. $Co^{2+}$ is represented by red circles. (B) Structure of TRPA1 (3J9P) with ankyrin repeats 12–16 shown in red, orange, blue, magenta, and gray.

in $H_2O$ for 20 min and were then washed twice using PBS (Sigma-Aldrich) to remove excess polylysine. 2 d after transfection, cells were washed once with PBS and once with HEPES-buffered saline solution (HBSS; containing [in mM] 1.8 $CaCl_2$, 1.0 $MgCl_2$-$6H_2O$, 4.0 KCl, 10 HEPES, 140 NaCl, and 5.0 D-glucose, pH 7.4) and transferred to the polylysine-coated coverslips in a 6-well tray containing HBSS. Attempts were made to minimize the exposure of cells to room light during this procedure.

### Western blot analysis

Cells were harvested 2 or 3 d after transfection and washed twice with PBS. For each wash, cells were collected by centrifugation at 900 *g* for 5 min at room temperature. Cell lysates were prepared by trituration of the cells in digitonin buffer (20 mM triethanolamine [Sigma-Aldrich], 300 mM NaCl [Sigma-Aldrich], 2 mM EDTA [Sigma-Aldrich], 20% glycerol [Fisher Scientific or Sigma-Aldrich], and 1% digitonin [Sigma-Aldrich] with Halt protease inhibitor cocktail [Fisher Scientific], pH 8.0) followed by 2-h incubation at 4°C on a tube rotator (Stein et al., 2006). After incubation, the cell lysate was centrifuged at 20,000 *g* for 15 min at 4°C. The lysate was transferred to a new tube and mixed with 1× volume of Laemmli sample buffer (Bio-Rad) with 5% β-mercaptoethanol (Bio-Rad). Proteins were separated by electrophoresis using either NuPAGE 4–12% Bis-Tris precast gels (Invitrogen) with MOPS SDS running buffer (50 mM MOPS, 50 mM Tris base, 0.1% SDS, and 1 mM EDTA) or Mini-Protean TGX 4–20% precast gels (Bio-Rad) and transferred to a PVDF membrane (Bio-Rad) using the semidry transfer method with Bjerrum and Schafer-Nielsen transfer buffer (40 mM Tris, 39 mM glycine, and 20% methanol, pH 9.2; Bjerrum and Schafer-Nielsen, 1986) with 0.037% SDS (Bio-Rad). Membranes were blocked for 1 h in TBS-T (20 mM Tris [Sigma-Aldrich], pH 7.6, 137 mM NaCl, and 0.1% Tween 20 [Fisher Scientific]) containing 5% nonfat dry milk (Milkman Instant Low-fat Dry Milk; Familiar Foods). Primary antibody was diluted in TBS-T plus nonfat dry milk, and the secondary antibody was diluted in TBS-T (anti–rabbit) or TBS-T plus nonfat dry milk (anti–goat). For anti-YFP antibody–probed images, polyclonal anti-GFP antibody (Torry Pine Biolabs) was used at a 1:5,000 dilution, and anti–rabbit IgG (KPL) was used at 1:30,000 as the secondary antibody. For anti-TRPV1 antibody–probed images, anti-TRPV1 antibody (P19; Santa Cruz Biotechnology) was used at a 1:500 dilution, and anti–goat IgG horseradish peroxidase (Santa Cruz Biotechnology, Inc.) was used at a 1:5,000 dilution. Membranes were developed using SuperSignal West Femto Max Sensitivity Substrate (Thermo Fisher Scientific), and images were obtained using a FluorChem 8000 (Alpha Innotech; Stein et al., 2006).

### Cell unroofing

We unroofed cells as reported elsewhere (see Gordon et al. in this issue). 4–48 h after transfected cells were transferred to coverslips in HBSS, coverslips were removed from the incubator and placed in our perfusion chamber on the microscope at room temperature (see Fig. 5 A). Gentle flow was used to wash with PBS (Sigma-Aldrich; 2 mM $CaCl_2$ [Sigma-Aldrich] and 1 mM $MgCl_2$ [Mallinckrodt], pH measured at 7.3 and not adjusted; sterile filtered through 0.22-µm membrane) for 15 min. The sonicator probe (Bronson Sonifier; 3-mm tapered tip) was then positioned in the chamber, with its tip ∼2 mm from the top of the coverslip. Polylysine (0.1 mg/ml in PBS; 30,000–70,000 mol wt; Sigma-Aldrich) was perfused through the chamber for 10 s, causing cells to expand their footprints and adhere more tightly to the coverslips. Swell buffer (a dilution of one part stabilization buffer to two parts water) was then rinsed through the chamber for 30 s, and stabilization buffer (70 mM KCl [Sigma-Aldrich], 30 mM HEPES [Sigma-Aldrich], and 1 mM $MgCl_2$ [Mallinckrodt]; initial pH measured at 5.2 and adjusted to 7.4 with KOH; sterile filtered through a 0.22-µm membrane) was used to rinse the chamber well. The vacuum line was then turned off, and the chamber was allowed to fill with as much stabilization buffer as possible without flowing over. A sonic pulse from the probe sonicator (Branson Sonifier 400 W) was given for 0.4 s with a power setting of 2. The probe was then removed from the chamber, and the experiment commenced.

### Labeling with C18-NTA and imaging

C18-NTA (stearoyl–nitrilotriacetic acid) was custom synthesized by Toronto Research Chemicals. It was made as 10-mM stock in DMSO and stored at −20°C. C18-NTA was diluted to 10 µM in stabilization buffer supplemented with 10 µM $CoSO_4$ and applied as described in Results.

Experiments with unroofed cells were performed using a Nikon TiE inverted microscope with a 60× (1.49 NA) oil immersion objective with the Nikon Perfect Focus system for preventing focal drift. Excitation for epifluorescence was provided by a xenon lamp (Sutter Lambda LS, 175 W) using filter sets for GFP (480/40-nm band-pass excitation filter and 535/50-nm band-pass emission filter), YFP (514/10-nm band-pass excitation filter and 575-nm long-pass emission filter), and L-ANAP (376/30-nm band-pass excitation filter and 485/40-nm emission filter). All imaging data were collected with Nikon NIS-Elements AR software controlling a Photometrics QuantEM 512SC Camera. ANAP emission spectra from cells were measured as above, but with a 425-nm long-pass emission filter in place of the band pass filter for ANAP, and a spectrograph (Acton SP2150; Princeton Instruments; 300 g/mm grating, blaze = 500) was placed between the microscope and the electron-multiplying CCD camera.

Image analysis was performed with ImageJ (Schneider et al., 2012). Typically, regions of interest were created surrounding individual cells, and nearby regions of interest were created in areas devoid of cells to represent the background. In all cases, the mean gray value of the background region was subtracted from the mean gray value of the cell regions. The fluorescence used to normalize the data were collected in the presence of EDTA to minimize quenching caused by binding of stray metal ions in the water to the NTA head group. Data were analyzed and plotted with Excel 2013 (Microsoft) and Igor Pro (WaveMetrics).

### Spectrophotometry and spectrofluorometry

Absorption spectra were recorded with a DU 800 spectrophotometer (Beckman Coulter), and fluorescence excitation and emission spectra were recorded with a Fluorolog 3 spectrofluorometer using FluorEssence software (HORIBA Jobin Yvon) as described elsewhere (Gordon et al., 2016). For emission spectra, 20 nM L-ANAP-ME (AsisChem Asis-0146) in stabilization buffer was placed in a 100-µl chamber of a 0.2 × 1-cm quartz cuvette and excited at 360 nm, and the emission spectrum was recorded from 400 to 700 nm. $Co^{2+}$-NTA was added at final concentrations of 0 to 200 mM from a stock solution of 200 mM $CoSO_4$ (Sigma-Aldrich) and 300 mM NTA (Sigma-Aldrich) made in stabilization buffer and pH adjusted to 7.4 with KOH. To account for the decrease in excitation and emission intensities caused by the optical density of the metal, observed fluorescence intensities of the sample were corrected for the inner filter effect according to the following equation (Lakowicz, 2006):

$$F_{ci} = F_{oi}\left[10^{(0.1*OD_{360}+0.5*OD_i)}\right],$$

where $F_{ci}$ and $F_{oi}$ represent the corrected and observed fluorescence intensities at *i*-nm wavelength, and $OD_{360}$ and $OD_i$ are the absorption of $Co^{2+}$-NTA recorded at 360- and *i*-nm wavelengths, respectively. The fluorescence resonance energy transfer (FRET) efficiency was then calculated using the equation

$$\text{FRET efficiency} = 1 - F_{Co}/F,$$

where $F$ and $F_{Co}$ are the corrected fluorescence intensities in the absence and presence of $Co^{2+}$, respectively.

### FRET: Theoretical framework

The dependence of FRET efficiency on the distance from the membrane (see Fig. 11 B) was calculated from the theoretical dependence of FRET efficiency on closest approach distance ($R_c$). For this calculation, we used Förster's distance-dependent model of energy transfer (Förster, 1949) as described for the FRET pair rhodamine B and $Co^{2+}$ (Gordon et al., 2016), with the following modifications. $R_0$ for ANAP and $Co^{2+}$-NTA was calculated as 12.8 Å based on our emission and absorption spectra of L-ANAP-ME and $Co^{2+}$-NTA (see Fig. 8 A), respectively, in stabilization buffer, our estimate of 0.22 for the quantum yield of ANAP in stabilization buffer (Fig. S3), and assuming $\kappa^2$ of 2/3 (Fung and Stryer, 1978; Loura, 2012). The density of C18-NTA-$Co^{2+}$ incorporated into the plasma membrane was assumed to be 0.002 molecules/Å$^2$ from our previous experiments with rhodamine B and C18-NTA-$Co^2$ (Gordon et al., 2016).

### Inside-out excised patch recordings

Currents were recorded at room temperature as previously described (Ufret-Vincenty et al., 2015) using filamented borosilicate glass pipettes (inner diameter 0.86 mm, outer diameter 1.5 mm, heat polished with a microforge to a resistance of 3.5–5.0 MΩ). Symmetric solutions were used for all recordings. Solutions were (in mM) 150 NaCl, 3 HEPES, and 0.2 EDTA, pH 7.2. Cells grown on 12-mm coverslips were placed in a 12-mm open configuration chamber. Excised, inside-out patches were held at 0 mV, and the potential was stepped to between −100 and 100 mV to drive currents through open channels. Solutions were perfused onto the cytosolic-facing side of the membrane patch by positioning the recording pipette directly in front of an open tube in a "sewer pipe" configuration of six tubes assembled on a rod controlled by a RSC-200 stepping motor (Bio-Logic Science Instrument). Currents were recorded using an EPC-10 amplifier and Patchmaster software (HEKA). Capsaicin was prepared as a 40-mM stock solution in ethanol, stored at 4°C, and diluted to 10 µM in recording solution immediately before use. Within each experiment, the same 10 µM capsaicin solution was used to make a 1 µM capsaicin solution, also in recording solution. All currents shown are capsaicin-activated currents; i.e., the current in recording solution (no capsaicin added) was subtracted from the current measured in the presence of the indicated concentration of capsaicin.

### Calcium imaging

Cells were grown on 25-mm coverslips, and then the coverslips were placed into a 35-mm dish with 2 ml working solution of 2 µM Rhod-2 AM (Life Technologies) in HBSS and incubated for 30 min at room temperature. Cells were then washed twice with HBSS and incubated in HBSS for another 30 min at room temperature. Fluorescence was imaged using a metal halide lamp (X-Cite, Series 120) for excitation with a 488/10-nm excitation filter and a 605/70-nm emission filter on a Nikon TE-2000U microscope equipped with an electron-multiplying CCD camera (QuantEM; Photometrics), which was controlled with MetaMorph software. The objective used was a 10× Nikon E Plan with NA of 0.25. Perfusion of the entire chamber was accomplished using open, gravity-driven reservoirs exiting through a micromanifold (Warner, MP Series) into the chamber. During perfusion, 100-ms exposures were collected at 0.5 Hz. 10 µM ionomycin was added to the chamber at the indicated time as a test for cell viability. Ionomycin was diluted from a 1 mM (DMSO) stock (stored at 4°C) into HBSS on the day of the experiment. ImageJ (Schneider et al., 2012) and Excel 2013 (Microsoft) were used for analysis of $Ca^{2+}$ imaging data.

### Lifetime measurements

Lifetime measurements were made as described previously (Gordon et al., 2016), with the following changes. A 375-nm laser was used for excitation, with a 390-nm long-pass filter for emission. 200 nM L-ANAP-ME was used for measurement either with no $Co^{2+}$ or with 20 mM $Co^{2+}$-NTA.

### Online supplemental material

Fig. S1 illustrates the amber codon suppression strategy used for introducing the noncanonical amino acid L-ANAP. Fig. S2 presents images illustrating our method for measuring spectra on the microscope as well as the calculated spectrum compared with spectra recorded on a fluorometer. Fig. S3 presents primary data used for determining the quantum yield of L-ANAP in our recording solution. Online supplemental material is available at http://www.jgp.org/cgi/content/full/jgp.201511531/DC1.

## RESULTS

Our approach to measuring the structure and dynamics of membrane proteins relative to the plasma membrane combines three methodologies: (1) amber codon suppression, (2) cell unroofing, and (3) tmFRET. Amber codon suppression was used to site-specifically label the protein with a fluorescent, noncanonical amino acid in the context of a native membrane. Cell unroofing was used to isolate just the plasma membrane of the cell for fluorescence measurements and provide solution access to the intracellular surface of the membrane. tmFRET was used to measure FRET between the fluorescent amino acid and metal ions bound to the membrane (Fig. 1 A). The combination of these three methods allowed us to measure distances of three residues in the N-terminal domain of TRPV1 relative to the membrane and changes in these distances that result from channel activation by capsaicin.

### Introducing a fluorescent, noncanonical amino acid using amber codon suppression

The power of using fluorescence to probe protein actions within the cell is limited by the specificity with which a protein can be labeled with a fluorophore in its native environment (the cell). For measuring the structure and dynamics of a protein, it is also important to use a small fluorophore attached to the protein with short linkers (Taraska and Zagotta, 2010). To achieve this specific fluorescent labeling with a small fluorophore, we used amber codon suppression to introduce the fluorescent, noncanonical amino acid L-ANAP (Chatterjee et al., 2013). We chose L-ANAP, a derivative of prodan, because of its small size and useful spectral properties (Lee et al., 2009; Chatterjee et al., 2013). By introducing a fluorophore as the side-chain of an amino acid, we eliminated the need for a linker whose distance from the protein backbone and flexibility reduces the empirical

sensitivity of FRET (Taraska et al., 2009b). This fluorescent amino acid can then be used as a FRET donor with a transition metal bound to the membrane as a FRET acceptor to measure distances relative to the plasma membrane.

An orthogonal amber suppressor tRNA/aminoacyl-tRNA synthetase pair has recently been described for incorporating L-ANAP into proteins in mammalian cells at positions encoded by the amber stop codon TAG (Chatterjee et al., 2013). L-ANAP was incorporated into GFP in mammalian cells by cotransfecting a plasmid encoding GFP with the TAG stop codon at position 40 (pEGFP-Y40TAG) with a plasmid encoding the tRNA/aminoacyl-tRNA synthetase pair (pANAP) and culturing cells with L-ANAP in the medium (Fig. S1). We tested a different, commercially available form of L-ANAP in our experiments that was supplied as a methyl ester (L-ANAP-ME; Fig. 2 A). The esterification of the carboxyl group of the amino acid facilitates entry of L-ANAP into cells, whereupon nonspecific esterases de-esterify it. Fig. 2 B (left column) shows a field of HEK293T/17 cells cotransfected with pEGFP-Y40TAG and pANAP, incubated with L-ANAP-ME, and imaged with bright field (top) or fluorescence microscopy. As

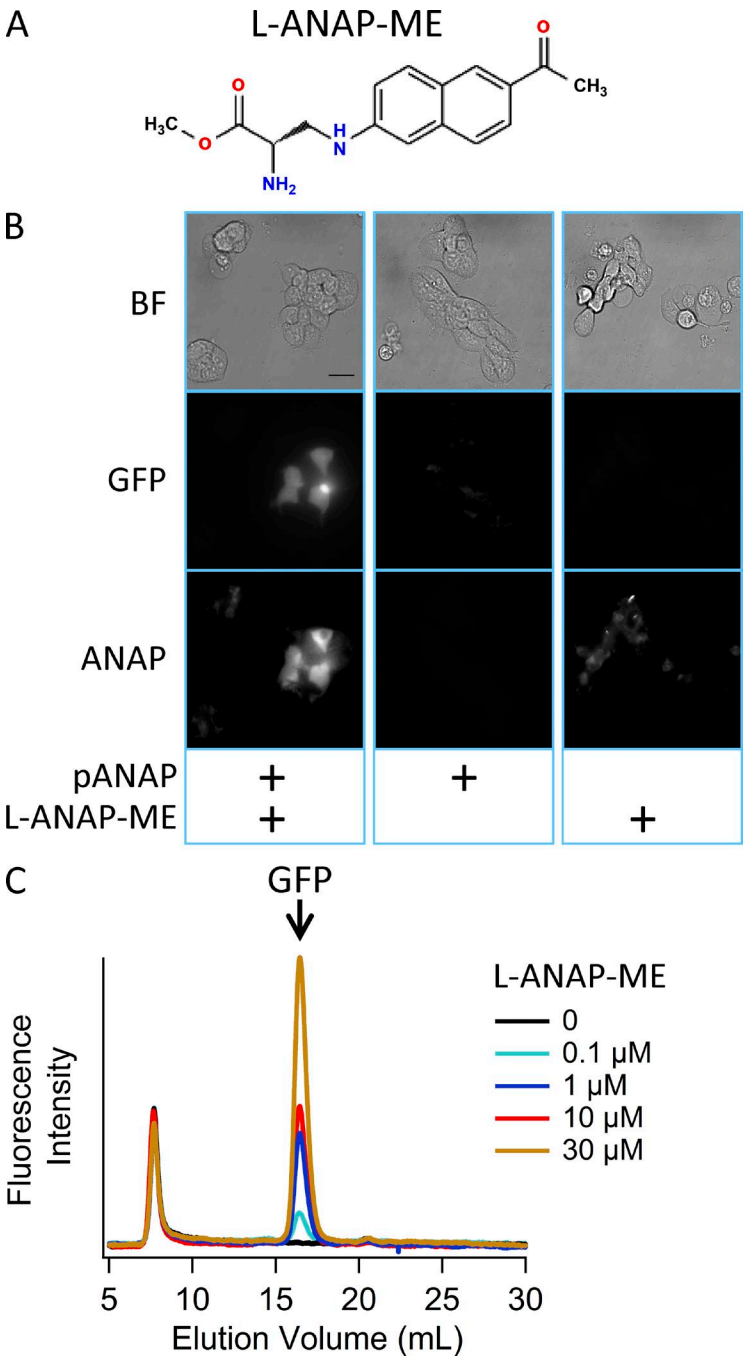


**Figure 2.** Incorporation of the noncanonical amino acid L-ANAP into GFP. (A) The structure of L-ANAP-ME, the noncanonical amino acid used in this study. (B) Incorporation of L-ANAP into GFP-Y40TAG requires coexpression with pANAP and the addition of L-ANAP-ME to the culture medium. Each column shows the same field of cells taken using bright field (BF) microscopy (top), epifluorescent microscopy with an excitation/emission cube appropriate for GFP (middle), or epifluorescent microscopy with an excitation/emission cube appropriate for ANAP (bottom). All cells were transiently transfected with a plasmid encoding GFP-Y40TAG. Cells were cotransfected with pANAP and/or cultured in the presence of L-ANAP-ME as indicated at the bottom. For all images using the same cube, the camera settings and lookup tables used were identical. (C) Fluorescence detection size-exclusion chromatograph showing GFP fluorescence versus elution volume for cleared cell lysates generated from cells transfected with GFP-Y40TAG and pANAP and cultured with various concentrations of L-ANAP-ME. The earliest peak corresponds to the void volume of the column, and its presence in control samples not expressing GFP indicates that it is not a specific protein signal.

for the published L-ANAP free acid, L-ANAP-ME was incorporated into GFP-Y40TAG as indicated by robust GFP fluorescence in many of the cells (Fig. 2 B, left column, middle row). As shown in Fig. 2 B (left column, bottom row), these cells also had increased ANAP fluorescence relative to the nonexpressing cells, consistent with incorporation of L-ANAP into GFP-Y40TAG. In contrast, cells transfected with the same two plasmids but cultured without L-ANAP-ME in the medium were not fluorescent in either ANAP or GFP color channels (Fig. 2 B, middle column). In addition, cells cultured with L-ANAP-ME but transfected with only pEGFP-Y40TAG, and not pANAP, showed little ANAP fluorescence and no GFP fluorescence (Fig. 2 B, right column), indicating that L-ANAP-ME was present in the cells, but only when both the tRNA/aminoacyl-tRNA synthetase pair and the noncanonical amino acid were present was L-ANAP incorporated into GFP-Y40TAG to produce a fluorescent protein.

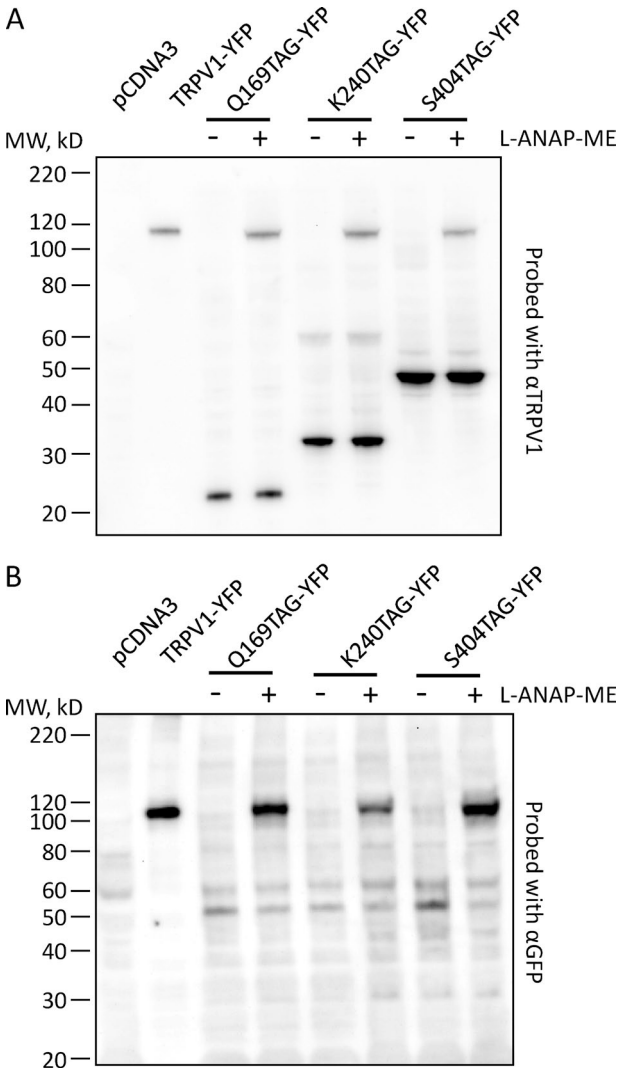


**Figure 3.** TRPV1-TAG-YFP constructs express as full-length protein with L-ANAP-ME. Western blots of cells cotransfected with pANAP and the indicated plasmids and cultured with (+) or without (−) L-ANAP-ME in the medium. (A) Blot was probed with an anti-TRPV1 antibody that recognizes and epitope in the N terminus of the channel sequence. The amount of TRPV1-YFP loaded on the gel was 40-fold less than the amount of the TAG mutations. (B) Blot was probed with an antibody that recognizes YFP. The amount of TRPV1-YFP loaded on the gel was 25-fold less than the amount of the TAG mutations. MW, molecular weight.

To determine the optimal concentration of L-ANAP-ME to include in the cell culture medium, we used fluorescence-detection size-exclusion chromatography (Kawate and Gouaux, 2006) to measure the amplitude of GFP fluorescence under different conditions. The cells were transiently transfected with pEGFP-Y40TAG and pANAP and cultured with various concentrations of L-ANAP-ME. Cleared cell lysate from each of these conditions was run on a gel filtration column on an HPLC equipped with a fluorescence detector, and the resulting chromatograms are shown in Fig. 2 C, which plots fluorescence intensity in the GFP color channel as a function of elution volume. GFP eluted at 16 ml (Fig. 2 C, arrow). No monodispersed signal was observed at this volume in cells cultured without L-ANAP-ME (black trace), consistent with our observations using fluorescence microscopy (Fig. 2 B, middle column), indicating that there is little or no mis-incorporation of other amino acids at the TAG stop codon. The GFP signal from the other conditions increased with the concentration of L-ANAP-ME in the medium, up to 30 µM (colored traces). At concentrations higher than this, highly fluorescent (in the ANAP color channel) precipitate was observed in the cells, and significant cell death occurred (not shown). For the remaining experiments, we used 20 µM L-ANAP-ME in the culture medium to balance between cell health and L-ANAP incorporation.

### Expression of L-ANAP–incorporated TRPV1 constructs as functional, capsaicin-activated channels

We used the cryoEM structure of TRPV1 (Liao et al., 2013) to select amino acid positions in the ARD into which we would introduce L-ANAP. We chose residue positions for L-ANAP incorporation that are predicted to be solvent exposed and to have a range of distances from the surface of the bilayer relative to the characteristic distance for tmFRET (∼13 Å; see Fig. 8). Based on these criteria, we chose three positions in TRPV1, Q169, and K240 in the ARD and S404 in the ARD-S1 linker. These positions were individually mutated to a TAG stop codon in TRPV1-YFP, with YFP fused to the C terminus as an additional fluorescence reporter.

During protein translation on ribosomes in mammalian cells, the probability that the noncanonical amino acid will be incorporated at the position encoded by the TAG amber stop codon is not 100% (Schmied et al., 2014). That is, sometimes when the translation machinery hits the TAG stop codon, translation stops and the polypeptide product dissociates from the ribosome.

Factors determining the efficiency of incorporation of noncanonical amino acids are not fully understood, although the concentration of loaded tRNA, the mRNA sequence, and the activity of release factors all likely play a role (Schmied et al., 2014). Whatever the mechanisms involved, the efficiency varies from construct to construct, such that successful incorporation of the noncanonical amino acid must be documented for every construct used.

We used Western blot analysis to determine the efficiency of incorporation of L-ANAP at positions 169, 240, and 404 of TRPV1. We transiently transfected HEK293T/17 cells with pANAP and a plasmid encoding TRPV1-Q169TAG-YFP, TRPV1-K240TAG-YFP, or TRPV1-S404TAG-YFP, with or without L-ANAP-ME supplemented in the culture medium. Detergent-solubilized cell lysate was then subjected to Western blot analysis using either an anti-TRPV1 antibody that recognizes an epitope in the N-terminal region of the channel (α-TRPV1) or an anti-GFP antibody that cross-reacts with YFP (α-GFP). A ∼110-kD band was observed with both α-TRPV1 (Fig. 3 A) and α-GFP (Fig. 3 B) for all three constructs in cells cultured with L-ANAP-ME (Fig. 3, lanes labeled +), but was absent from cells cultured in the absence of L-ANAP-ME (Fig. 3, lanes labeled −). The band appeared at the same size as that observed for wild-type TRPV1-YFP and was not observed in lysate from pcDNA3-transfected cells (Fig. 3), indicating that it represents full-length TRPV1-YFP. The Western blot with α-TRPV1 also revealed a prominent lower molecular weight band in each of the constructs at about the size predicted for protein truncated at the TAG stop codon. These results indicate that L-ANAP was incorporated at each of these positions, but with somewhat poor efficiency.

We next examined whether L-ANAP–incorporated channels were present on the plasma membrane as functional, capsaicin-activated channels. $Ca^{2+}$ imaging was performed with Rhod-2–loaded cells transiently transfected with pANAP and TRPV1-Q169TAG-YFP, TRPV1-K240TAG-YFP, or TRPV1-S404TAG-YFP and cultured with L-ANAP-ME. We found that 1 µM capsaicin produced a robust rise in intracellular calcium for all three constructs (Fig. 4 A). For a more direct measurement, inside-out patches were excised from cells selected on the basis of YFP fluorescence. Patches were held at 0 mV and jumped to potentials between −100 mV and 100 mV, in steps of 20 mV. All three constructs produced small, outwardly rectifying currents when exposed to 1 µM capsaicin (Fig. 4 B). The currents with 1 µM capsaicin were nearly as large as those elicited by 10 µM capsaicin for TRPV1-Q169TAG ($I_{1\ \mu M}/I_{10\ \mu M}$ = 1.1 ± 0.66 µM; $n$ = 3) and TRPV1-S404TAG ($I_{1\ \mu M}/I_{10\ \mu M}$ = 0.80 ± 0.36 µM; $n$ = 5), but were smaller for TRPV1-K240TAG ($I_{1\ \mu M}/I_{10\ \mu M}$ = 0.21 ± 0.12 µM; $n$ = 3). These data indicate that the $EC_{50}$ of these channels for activation by capsaicin was not appreciably higher than that expected for wild-type TRPV1 ($EC_{50}$ ≈ 1 µM; Collins and Gordon, 2013). We conclude that TRPV1 channels with L-ANAP incorporated at each of the three positions were functional, capsaicin-activated, and present on the plasma membrane.

### Unroofing cells to isolate the plasma membrane and access the intracellular surface

Cell unroofing is an established method for providing access to the intracellular surface of the plasma membrane in isolation from organelles and soluble cellular components (Heuser, 2000). In brief, adherent cells are swollen with hypotonic solution and their dorsal surface

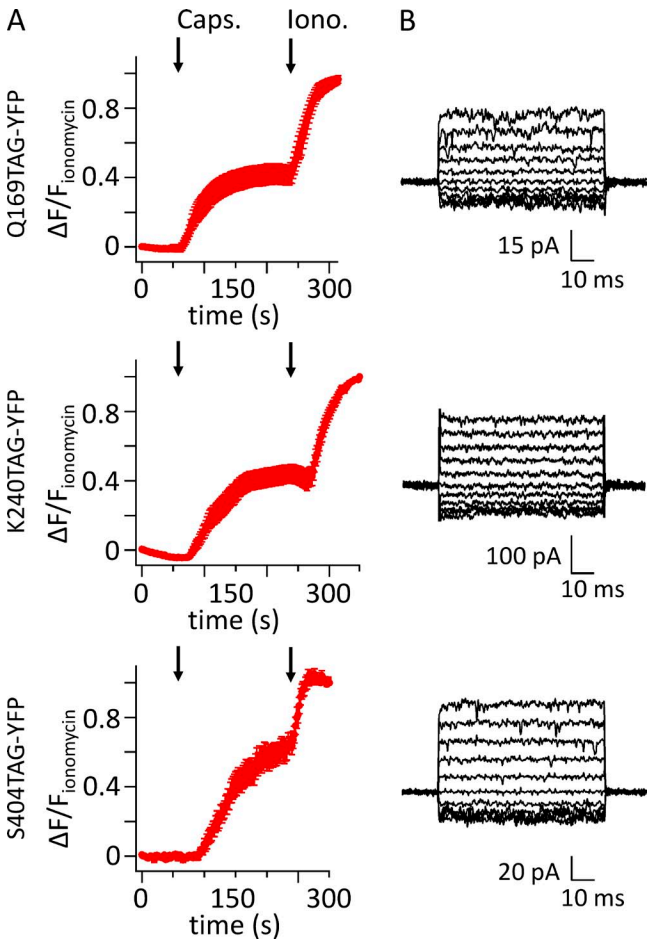


**Figure 4.** L-ANAP–incorporating TRPV1-TAG-YFP channels retain functional properties. Cells were cotransfected with pANAP and a plasmid encoding TRPV1-Q169TAG-YFP, TRPV1-K240TAG-YFP, or TRPV1-S404TAG-YFP, as indicated, and were cultured with L-ANAP-ME in the medium. (A) Mean fluorescence data from cells transfected as described and loaded with the $Ca^{2+}$ indicator Rhod-2-AM. 1 µM capsaicin (Caps.) was applied at 60 s, and ionomycin (Iono.) was applied at 240 s, as indicated by the arrows. Data represent means of 11, 6, and 10 cells for TRPV1-Q169TAG-YFP, TRPV1-K240TAG-YFP, and TRPV1-S404TAG-YFP, respectively. (B) Currents recorded in response to 1 µM capsaicin in inside-out excised patches held at 0 mV and jumped to potentials from −100 to 100 mV in steps of 20 mV. Currents in the absence of capsaicin were subtracted.

disrupted by a single pulse with a probe sonicator positioned just above the coverslip, leaving behind the ventral plasma membrane free from organelles and other soluble components. To image the same cells in a field before and after unroofing, we mounted the sonicator probe directly on the microscope stage, as shown in Fig. 5 A. An example of unroofing in cells transfected with TRPV1-YFP is shown in Fig. 5 (B and C). Initially, the cells were intact and can be seen as a clump with bright-field microscopy (Fig. 5 B, left). Epifluorescent imaging revealed that the TRPV1-YFP fusion was expressed in a subset of the cells and localized to both the plasma membrane and intracellular membranes, likely endoplasmic reticulum (Fig. 5 B, middle). Total internal reflection fluorescence (TIRF) imaging of the same field allowed visualization of the TRPV1-YFP exclusively or primarily in the ventral plasma membrane (Fig. 5 B, right). After application of a single pulse from the probe sonicator positioned above the cells, there was little or no indication of the cells that could be observed with bright-field imaging (Fig. 5 C, left). In contrast to what was observed with intact cells (Fig. 5 B), the epifluorescent and TIRF images were nearly identical after unroofing (Fig. 5 C, middle and right). In the absence of the soluble contents, organelles, and dorsal plasma membrane, all that remained adhered to the coverslip localized to within the TIRF imaging evanescent field. These data indicate that unroofing of cells expressing a fluorescent membrane protein is a useful method for isolating the ventral plasma membrane from other cellular contents, preserving those proteins in the membrane, and exposing the intracellular surface of the bilayer.

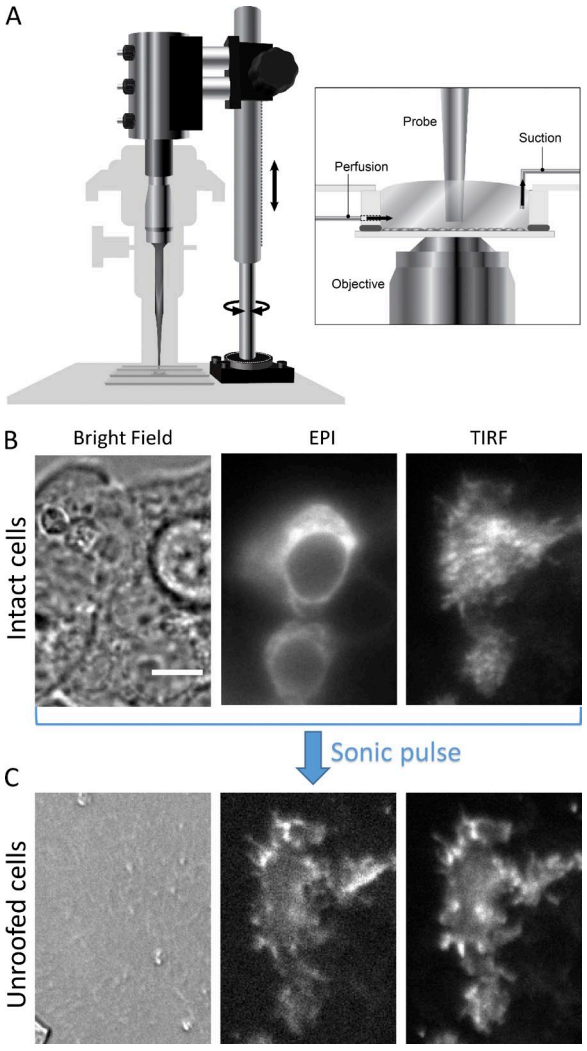


**Figure 5.** Cell unroofing setup and process. (A) Diagram of the experimental setup used to unroof cells in a chamber on the microscope stage (see Materials and methods). (B) A field of intact HEK293T/17 cells transiently transfected with TRPV1-YFP and imaged with bright field, epifluorescence (EPI), or TIRF microscopy, as indicated. (C) The same field of cells as in B after the cells were unroofed. The scale bar shown in the left panel of B is 10 µm and applies to all images in B and C.

Channels with ANAP incorporated could also be visualized in the unroofed cells. Fig. 6 A shows a field of unroofed cells transfected with TRPV1-Q169TAG-YFP and pANAP and cultured with L-ANAP-ME in the medium. One cell clearly shows both ANAP and YFP fluorescence, consistent with a TRPV1-Q169TAG-YFP channel in the plasma membrane that has incorporated L-ANAP. However, we found many other cells with weak background fluorescence in the ANAP channel that did not show corresponding YFP fluorescence (Fig. 6 A). This background fluorescence was found to bleach much more rapidly (compare blue trace to green and pink traces in Fig. 6 B). A 10-s prebleaching step at the beginning of the experiment eliminated the background fluorescent signal without greatly diminishing the ANAP signal, allowing us to isolate just the ANAP fluorescence from the channels (Fig. 6 A).

The peak of the L-ANAP emission spectrum is sensitive to its environment, shifting toward shorter wavelengths in more hydrophobic solvents (Fig. S2; Lee et al., 2009; Chatterjee et al., 2013). We selected amino acid positions 169, 240, and 404 to be in an aqueous environment, based on the cryoEM structure of TRPV1 (Liao et al., 2013). We addressed the environment of L-ANAP incorporated into the three sites on TRPV1 by measuring the emission spectra of cells expressing these constructs using a spectrograph mounted between the microscope and the camera. Using an ANAP-appropriate excitation filter, but with a long-pass emission filter, we recorded emission spectra for each of the three constructs (Fig. 7, red traces). The black trace shows the spectrum of L-ANAP-ME conjugated to an agarose bead in recording solution measured using the same microscope configuration, as illustrated in Fig. S2 A. Within the accuracy of our system, the spectrum of L-ANAP incorporated into TRPV1 was similar to that of L-ANAP-ME conjugated to beads in the same solution. These data support our assumption that L-ANAP

incorporated into positions 169, 240, and 404 appears to be solvent exposed.

An examination of the L-ANAP emission spectrum for TRPV1-Q169TAG-YFP revealed a second peak centered at 527 nm (Fig. 7 A). We hypothesized that this could reflect FRET between L-ANAP and the YFP fused to the C terminus of the construct. Indeed, the emission spectrum of TRPV1-Q169TAG-YFP (Fig. 7 A, red trace) can be fitted by the sum of two components (Fig. 7 A, dashed black trace), L-ANAP (black trace) and YFP (blue trace). FRET between YFP at the N terminus of TRPV1 and CFP at the C terminus of TRPV1 has been previously reported (De-la-Rosa et al., 2013). Our data suggest that, of the three positions into which we incorporated L-ANAP, Q169 may be the closest to YFP fused to the C terminus.

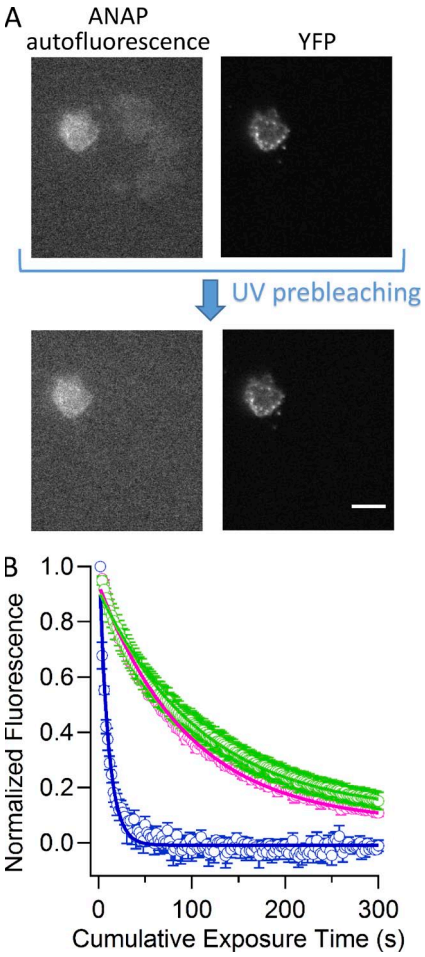


**Figure 6.** Fluorescent TRPV1 channels in unroofed cells. (A) Epifluorescent images of the same field of unroofed cells transfected with TRPV1-Q169TAG-YFP and pANAP and cultured with L-ANAP-ME in the medium in the ANAP color channel (left) and the YFP color channel (right). The top images show the initial data collected for this field. The bottom images show the field after a 10-s prebleaching UV exposure. The scale bar applies to all images and is 10 µm. (B) Collected data representing the dependence of fluorescence intensity in the ANAP color channel on cumulative time exposed to ANAP excitation light. Blue points represent YFP-negative cells, pink points represent TRPV1-K240TAG-YFP–expressing cells, and green points represent TRPV1-S404TAG-YFP–expressing cells. Solid curves are fits with a single exponential with a time constants of 10 s ($n = 5$ cells), 100 s ($n = 3$ cells), and 110 s ($n = 6$ cells) for YFP negative, TRPV1-K240TAG-YFP, and TRPV1-S404TAG-YFP, respectively. Error bars represent the SEM.

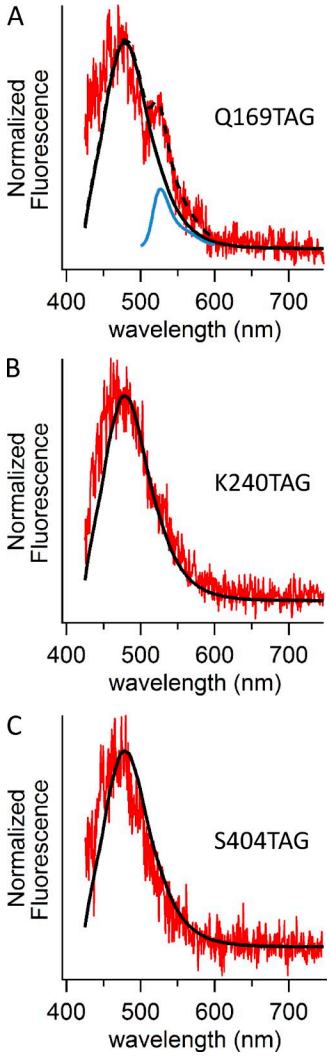


**Figure 7.** Fluorescence emission spectra from cells expressing L-ANAP–incorporating TRPV1 channels. (A–C) Emission spectra for unroofed cells transfected with pANAP and TRPV1-Q169TAG-YFP (A), TRPV1-K240TAG-YFP (B), or TRPV1-S404TAG-YFPv and cultured with L-ANAP-ME. Spectra were acquired as described in Fig. S2 but using the excitation cube appropriate for ANAP with the band-pass emission filter replaced by a 405-nm long-pass emission filter. The red traces represent the mean emission spectra from three unroofed cells, normalized to their peak before averaging. The black traces are from L-ANAP-ME conjugated to beads, also shown in Fig. S2 B. The dashed trace in A represents a fit to the cell data (red) by the sum of the L-ANAP-ME spectrum from the beads and a spectrum of YFP (blue), measured separately.

### Spectral properties of L-ANAP make it an ideal donor for tmFRET with $Co^{2+}$

tmFRET is a powerful method for measuring distances between a small-molecule fluorophore and a nonfluorescent transition metal (Taraska and Zagotta, 2010). Transition metal ions such as $Co^{2+}$, $Cu^{2+}$, and $Ni^{2+}$ absorb visible light and can therefore accept energy transfer from a nearby donor fluorophore and quench the donor's fluorescence (Latt et al., 1970, 1972; Horrocks et al., 1975; Richmond et al., 2000; Sandtner et al., 2007; Taraska et al., 2009a,b; Yu et al., 2013). The degree of quenching is a direct measure of FRET efficiency. FRET efficiency is steeply dependent on distance between the donor and acceptor, allowing tmFRET to serve as a ruler for intra- and intermolecular distances. The main advantages of tmFRET over classical FRET methods are (a) $R_0$ is very short (~10–20 Å), allowing short-range interactions to be studied; (b) the transition metals have multiple transition dipoles, reducing the orientation dependence of FRET; (c) the metals can be reversibly bound to native and introduced binding sites on the protein or the membrane; and (d) different metals have different absorption properties, and therefore $R_0$ values, allowing the choice of metal to be tuned to the distance of interest.

To match L-ANAP as a tmFRET donor with an appropriate transition metal acceptor, the emission spectrum of L-ANAP-ME was compared with the absorption spectra of several transition metals. The absorption spectra of transition metals can be affected by their chelation state (Reddy, 2010) and are shown in Fig. 8 A for $Co^{2+}$ (red), $Cu^{2+}$ (blue), and $Ni^{2+}$ (magenta) bound to NTA. Although all three transition metal ions had absorption spectra that overlap with the emission spectrum of L-ANAP-ME, we chose $Co^{2+}$ for its significant overlap with L-ANAP-ME fluorescence. The overlap between the emission spectrum of ANAP and the absorption spectrum of $Co^{2+}$-NTA, together with the quantum yield of ANAP (0.22; Fig. S3), predicts an $R_0$ of 12.8 Å for mobile randomly oriented donors and acceptors ($\kappa^2 = 2/3$; Fung and Stryer, 1978; Loura, 2012).

To demonstrate tmFRET between ANAP and $Co^{2+}$, we measured the energy transfer between L-ANAP-ME and $Co^{2+}$-NTA in solution. Because $Co^{2+}$ is a nonfluorescent acceptor, energy transfer can be seen as a decrease in the fluorescence of the donor (ANAP). As predicted, after correction for an inner filter effect, the emission intensity of ANAP was decreased by increasing concentrations of $Co^{2+}$-NTA, with little or no change in the shape of the emission spectrum (Fig. 8 B). The corrected emission intensity was plotted as a function of $Co^{2+}$-NTA concentration, giving 50% quenching at 20 mM $Co^{2+}$-NTA (Fig. 8 C). The efficiency of energy transfer is simply the fraction of fluorescence quenched upon addition of $Co^{2+}$ ($E = 1 - F_{CO}/F$). The efficiency of energy transfer can also be estimated from the decrease in the fluorescence

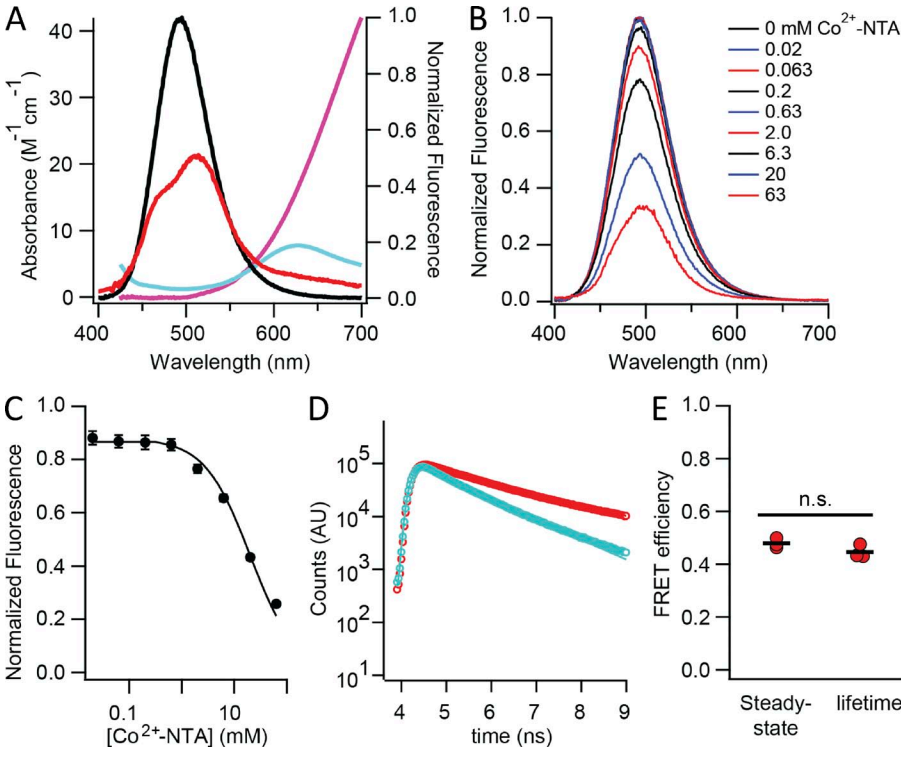


**Figure 8.** Spectral properties of L-ANAP-ME and $Co^{2+}$-NTA make them an ideal FRET pair for measuring small distances on the order of 10–20 Å. (A) The emission spectrum from L-ANAP-ME conjugated to the bead (black) overlaid on the absorption spectra of $Co^{2+}$-NTA (red), $Cu^{2+}$-NTA (blue), and $Ni^{2+}$-NTA (magenta). (B) Solution quenching of L-ANAP-ME by $Co^{2+}$-NTA. The fluorescence intensities at 490 nm were measured in various concentrations of $Co^{2+}$-NTA in stabilization buffer in a fluorometer. All curves were normalized to their maximum fluorescence intensity after inner filter effect correction and background subtraction. Smooth curve is a fit with the Hill equation with the following parameters: $K_{1/2}$ = 25 mM and Hill coefficient = −1. (C) Concentration dependence of quenching of L-ANAP-ME in solution by $Co^{2+}$-NTA (points) fitted with the Hill equation (black curve). (D) Fluorescence lifetime measurements of L-ANAP-ME in the absence (red circles) and presence (blue circles) of 20 mM $Co^{2+}$-NTA. Best fits to the data with a single exponential give time constants of 1.94 and 1.07 ns without and with $Co^{2+}$-NTA, respectively. AU, arbitrary units. (E) Energy transfer efficiencies estimated with steady-state and lifetime fluorescence measurements. The mean for each group is shown by the black line. n.s., no statistically significant difference between the groups ($P > 0.05$).

lifetime of fluorophore in the presence of quencher ($E = 1 - \tau_{CO}/\tau$). Indeed 20 mM $Co^{2+}$-NTA caused a dramatic decrease in ANAP fluorescence lifetime (Fig. 8 D). The efficiency of energy transfer calculated from lifetime measurements was not significantly different from the efficiency calculated from steady-state quenching (Fig. 8 E). In addition, the quenching by transition metals has been shown to exhibit the steep distance and metal dependence predicted for FRET (Latt et al., 1972; Taraska et al., 2009a,b; Yu et al., 2013). Although we cannot rule out a small contribution from other forms of energy transfer, these results are consistent with FRET being the primary mechanism for fluorescence quenching by transition metals.

### tmFRET measurements between L-ANAP incorporated into TRPV1 and $Co^{2+}$ bound to the plasma membrane

We next examined whether we could measure tmFRET between L-ANAP incorporated into TRPV1 and $Co^{2+}$ bound to metal-binding sites on the intracellular surface of the plasma membrane in unroofed cells. We have previously shown that endogenous metal binding sites on the intracellular surface of the plasma membrane are too low affinity and at too low a density to exhibit appreciable tmFRET with the membrane-resident fluorophore octadecyl rhodamine B (R18), which has an $R_0$ of 12.0 Å (Gordon et al., 2016). To overcome this challenge, we have developed an approach to decorate the membrane of unroofed cells with a high density of high-affinity metal binding sites (Gordon et al., 2016). We used a custom-synthesized lipid with a metal-chelating head group, stearoyl–nitrilotriacetic acid (C18-NTA; Fig. 9). C18-NTA can be applied to the unroofed cells via perfusion, and it spontaneously partitions into the bilayer. Furthermore, C18-NTA appears to remain in the bilayer on the time scale of our experiments (1 h or more). Using tmFRET between the R18 and $Co^{2+}$ bound to C18-NTA (C18-NTA-$Co^{2+}$), we determined the density of C18-NTA in the bilayer (~0.002 molecules/Å$^2$ under our experimental conditions) and the affinity of $Co^{2+}$ for C18-NTA (<<1 µM; Gordon et al., 2016). These data provide the foundation for measuring distances between L-ANAP incorporated into TRPV1 and $Co^{2+}$ bound to C18-NTA in the intracellular leaflet of the cell plasma membrane.

To measure tmFRET, we measured the fluorescence of unroofed cells expressing L-ANAP–incorporated TRPV1 channels before and after perfusion of 1 µM $Co^{2+}$ into the bath. As expected, application of 1 µM $Co^{2+}$ had little or no effect before treatment with C18-NTA (Fig. 9, columns 1 and 2). However, as shown in Fig. 9 A (column 3), 1 µM $Co^{2+}$ applied after treatment with C18-NTA produced a small reduction in L-ANAP fluorescence for TRPV1-Q169TAG, the position expected to be the farthest from the plasma membrane. A larger reduction of L-ANAP fluorescence with $Co^{2+}$ application was observed in TRPV1-K240TAG (Fig. 9 B, column 3), a position expected to be located at an intermediate distance from the membrane. Finally, the greatest reduction in L-ANAP signal with $Co^{2+}$ application was observed in TRPV1-S404TAG, in which the incorporated L-ANAP is expected to be closest to the plasma membrane (Fig. 9 C, column 3). Importantly, quenching was not reversed by >10 min of washing unroofed cells with $Co^{2+}$-free stabilization buffer, but was reversed by 5–10 min of washing with stabilization buffer supplemented with 10 mM EDTA (Fig. 9, column 5). These data are consistent with the expected irreversible (over the time course of our experiments) partitioning of C18-NTA into the plasma membrane and high-affinity binding of $Co^{2+}$ to NTA and support our interpretation that $Co^{2+}$ bound to C18-NTA indeed decorated the surface of the membrane. The YFP fused to the C terminus of TRPV1, expected to be distant from the plasma membrane and in the same position in each of the three constructs, showed little or no reduction in fluorescence with $Co^{2+}$ treatment (Fig. 9, column 3). These data are summarized for multiple cells in Fig. 10 A and indicate that tmFRET between an L-ANAP incorporated membrane protein and a transition metal bound to C18-NTA can report distance changes relative to the membrane.

We also asked whether we could discern a change in the position of L-ANAP relative to the membrane upon channel activation. We applied a saturating concentration of the TRPV1 agonist capsaicin in a solution also containing 1 µM $Co^{2+}$. As shown in Fig. 9 (column 4) and Fig. 10 B, capsaicin did not alter the tmFRET signal for any of the constructs. Because our solutions contained no added $Ca^{2+}$, $Ca^{2+}$-dependent desensitization to capsaicin was not a concern. These data suggest that if any rearrangement of the N-terminal domain relative to the membrane occurs during activation, it is smaller than the resolution of our approach.

## DISCUSSION

In this paper, we show that tmFRET is a powerful approach for elucidating the structure of protein domains relative to the cell plasma membrane. By unroofing cells to expose the intracellular surface of the plasma membrane, we could decorate it with a high density of high-affinity $Co^{2+}$-binding sites. To test the approach, we chose three sites for incorporating the fluorescent noncanonical amino acid L-ANAP in the N-terminal region of TRPV1. The FRET efficiencies for quenching of L-ANAP by membrane-bound $Co^{2+}$ decreased with increasing predicted distance of the sites from the membrane. Interestingly, L-ANAP at position 169 also acted as a FRET donor for the C-terminal fused YFP. The dependence of the tmFRET efficiency on distance indicates that tmFRET with the membrane can be used to

measure both the structure and dynamics of membrane proteins. Although we did not observe capsaicin-dependent changes in tmFRET for the three constructs, the cryoEM structures of the apo state and activating toxin-bound state of TRPV1 indicate that little activation-dependent change in the position of the ARDs relative to the membrane is expected (Cao et al., 2013; Liao et al., 2013).

The experimental and theoretical distance dependences for tmFRET relative to the membrane are shown in Fig. 11. The distances for the ANAP sites were estimated from the position of Cβ in the published cryoEM structure of TRPV1 (Liao et al., 2013) relative to the estimated position of the cytoplasmic surface of the plasma membrane (Fig. 11 A, dashed line). The experimental FRET efficiencies were calculated as $E = 1 - F_{CO}/F$, and the theoretical efficiencies were calculated based on a model of FRET in two dimensions (Fig. 11 B; Fung and Stryer, 1978). The model assumes random arrangement of acceptors in the membrane at a density of 0.002 molecules/Å$^2$ as determined from other experiments (Gordon et al., 2016).

Although our experiments reveal a decrease in tmFRET efficiency with increased distance, our measurements deviated from the theoretical distance dependence, particularly at longer distances. The FRET efficiency we measured for L-ANAP at position 169 is especially problematic, as essentially no FRET signal is predicted for a site so distant from $Co^{2+}$ bound to the plasma membrane. The anomalously high FRET efficiency could not have been caused by $Co^{2+}$ binding to off-target locations within TRPV1 or any other part of the plasma membrane, as it was observed only after treatment of unroofed cells with C18-NTA (Fig. 9 A, column 2 compared

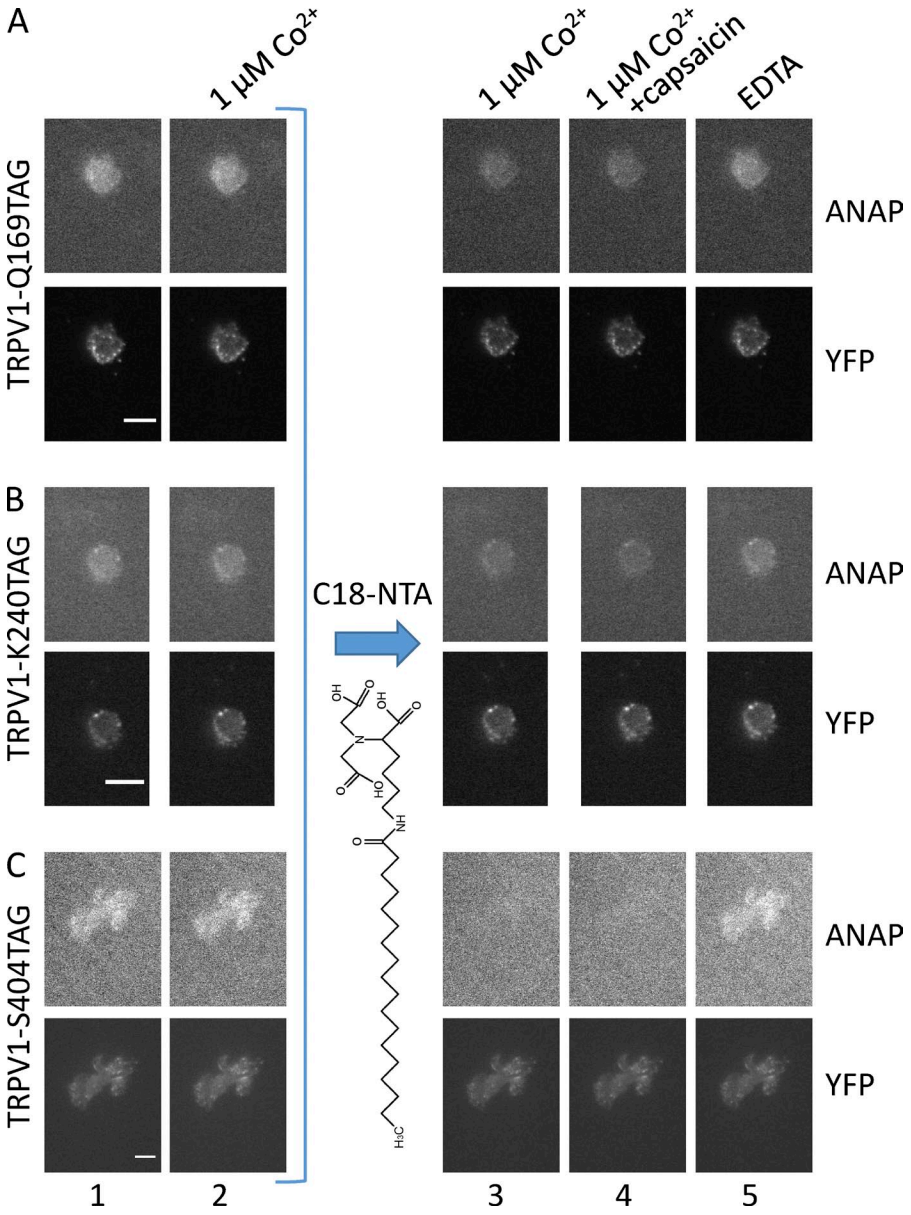


**Figure 9.** tmFRET occurs between L-ANAP incorporated into TRPV1 and $Co^{2+}$ bound to C18-NTA in the membrane. (A–C) ANAP and YFP fluorescence from unroofed cells co-transfected with pANAP and TRPV1-Q169TAG-YFP (A), TRPV1-K240TAG-YFP (B), and TRPV1-S404TAG-YFP (C) and cultured with L-ANAP-ME in the medium. Images were acquired with an ANAP-appropriate cube and a YFP-appropriate cube as indicated. For each field, the same camera settings and lookup table were used for all images in the same color channel. Epifluorescence images were acquired in the sequence shown starting with the initial fluorescence with no added $Co^{2+}$ (column 1) and then in the presence of 1 μM $Co^{2+}$ (column 2). Subsequently, the unroofed cells were incubated in C18-NTA as described in Materials and methods, and images were acquired in the presence of 1 μM $Co^{2+}$ (column 3), 1 μM $Co^{2+}$ with capsaicin (column 4), and EDTA (column 5). Scale bars for all panels are 10 μm.

with column 3). The apparent decrease in distance dependence could have several possible origins. (1) In addition to incorporating into the membrane, C18-NTA may bind to another part of the channel or nearby site. This site would have to have nearly irreversible binding of C18-NTA (because the quenching of $Co^{2+}$ lasts more than an hour) and be within ~12–15 Å of L-ANAP at position 169 and distant from the C-terminal YFP. (2) Background fluorescence from L-ANAP (unincorporated or incorporated in other membrane proteins) or from other fluorescent molecules might also be quenched by $Co^{2+}$ bound to C18-NTA. However, because we saw essentially no fluorescence after prebleaching from membranes not expressing channels, contributions from quenching of this background would be negligible. (3) Heterogeneity of the position of C18-NTA perpendicular to the bilayer or deformations of the bilayer itself might bring the $Co^{2+}$ acceptors closer to the distal end of the ARD. (4) The structure of the ARD of TRPV1 in the membrane may differ from the cryoEM structure of TRPV1 in amphipols (Cao et al., 2013; Liao et al., 2013). (5) The ARD of TRPV1 might be highly dynamic with occasional sojourns into a conformation where L-ANAP is closer to the membrane. Because of the highly nonlinear nature of FRET, these closest approach distances will be more highly represented in the FRET measurements. Significant dynamics of the ARDs might be expected, given the very pronounced effects of mutations

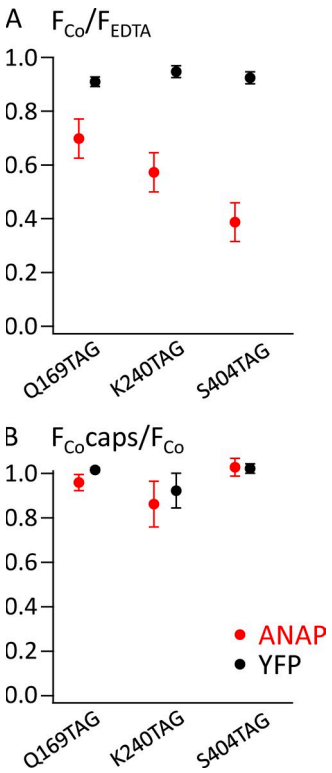


**Figure 10.** tmFRET of L-ANAP incorporated into TRPV1 decreases with expected distance from the surface of the plasma membrane but does not change in response to capsaicin. (A) ANAP (red circles) or YFP (black circles) fluorescence from the indicated channels acquired after incubation with C18-NTA. The fluorescence is expressed as the ratio of the background-subtracted mean intensity in the presence of 1 µM $Co^{2+}$ to that in the presence of EDTA, all in the absence of capsaicin. (B) No change in quenching of ANAP by $Co^{2+}$ was observed upon addition of capsaicin (caps). The ratio of the fluorescence in $Co^{2+}$ in the presence of capsaicin relative to the fluorescence in $Co^{2+}$ in the absence of capsaicin is plotted for ANAP and YFP for the indicated mutants. Error bars represent the SEM.

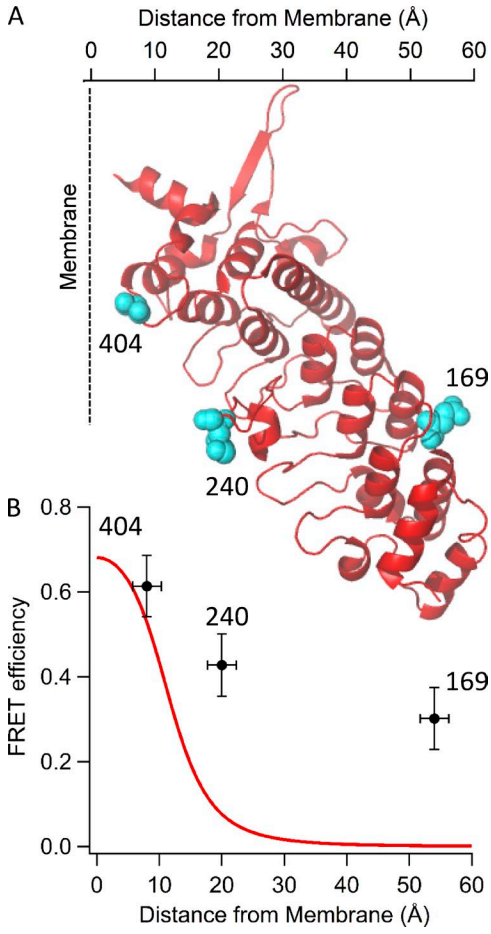


**Figure 11.** Experimental and theoretical distance dependence of tmFRET with the membrane. (A) The cryoEM structure of the ARD of TRPV1 is shown oriented relative to the expected intracellular surface of the plasma membrane. The three amino acids replaced by L-ANAP in this study are shown as cyan spheres, with the distance of each from the surface of the plasma membrane indicated on the abscissa. (B) Relationship between the FRET efficiency and distance from the surface of the plasma membrane. The points represent the experimentally determined FRET efficiency calculated from quenching of L-ANAP incorporated into each position by $Co^{2+}$ bound to C18-NTA on the plasma membrane. The position of the membrane surface and its uncertainty were estimated as the mean and standard deviation of the *z* coordinate of the charged atoms of amino acids (K431, R432, R491, R557, and K579) in the cryoEM structure (Cao et al., 2013; Liao et al., 2013). The error bars for FRET efficiency are the SEM of the quenching measurements. The smooth curve is the theoretical efficiency calculated based on a model of FRET in two dimensions (Fung and Stryer, 1978).

and posttranslational modifications in the ARDs on channel gating (Lishko et al., 2007; Myers et al., 2008; Salazar et al., 2008; Yao et al., 2011). Furthermore, the first two ankyrin repeats in the TRPV1 cryoEM structure (including position 169) could not be resolved and were instead modeled based on the crystal structure of the isolated ARD of TRPV1 (Lishko et al., 2007; Liao et al., 2013). The absence of these domains in the cryoEM structure could arise from mobility or conformational heterogeneity. The shallower-than-expected distance dependence we observed could arise from one or a combination of these origins. Whatever the origin, however, our experiments demonstrate that tmFRET can be used to measure difference in distances between sites on a membrane protein and the surface of the plasma membrane.

Comparing the ARDs in TRPV1 to those in TRPA1 shows significant differences in the orientation of the ARDs relative to the membrane in the two channels (Cao et al., 2013; Liao et al., 2013; Paulsen et al., 2015). In TRPV1, the ARDs are nearly parallel to the membrane, emanating from the transmembrane domain like the blades of a propeller (Fig. 1 A). In TRPA1, the ARDs extend almost perpendicularly from the membrane, like columns, organized around a central C-terminal coiled-coil domain (Fig. 1 B). The ARDs shown in Fig. 1 B are believed to correspond to repeats 12–15 of TRPA1, with the more distal repeats perhaps forming an inverted cap (not shown) around the column and repeats 12–15 (Paulsen et al., 2015).

L-ANAP has several properties that make it ideal for these experiments. The fluorophore of L-ANAP, based on prodan, is small and attached to the β-carbon of the amino acid (Fig. 2 A), so that its location faithfully represents that of the protein backbone. The small size of L-ANAP might also be important to preserve the function of some membrane proteins. The environmental sensitivity of L-ANAP may be useful for measuring changes in environment and does not interfere with measuring the FRET efficiency with the fluorescence before and after application of the transition metal. L-ANAP is excited with a peak wavelength of 360 nm (Chatterjee et al., 2013), long enough to be compatible with standard microscope optics. For such a small fluorophore, it is relatively bright (extinction coefficient = 19,500 $M^{-1}cm^{-1}$ and quantum yield = 0.22; Fig. S3). Although modest, accumulation of L-ANAP-ME, the methyl ester version we used, did occur in many cells (Fig. 2 B, right). However, the fluorescence due to L-ANAP was much greater in cells transfected with a TAG construct and pANAP than in those in which pANAP was absent (Fig. 2 B, left). The methyl ester version of L-ANAP produced significant toxicity for cells cultured in 100 µM L-ANAP-ME (unpublished data), but fortunately this was above the level required for successful incorporation in GFP-TAG and TRPV1-TAG constructs.

Although quenching of a fluorophore by metal can occur through mechanisms other than FRET, numerous lines of evidence support a FRET mechanism for the quenching of L-ANAP by $Co^{2+}$ that we observed. Collisional quenching or static quenching can occur but require diffusive encounters between fluorophore and quencher during the lifetime of the fluorophore excited state (collisional quenching) or complex formation between the fluorophore and the quencher (static quenching; Lakowicz, 2006). Diffusion rates for lipids in the cell membrane are very slow (∼2 $\mu m^2 s^{-1}$) with respect to the lifetime of L-ANAP (∼2 ns in stabilization buffer; Fig. 8 D). Complex formation between $Co^{2+}$ bound to C18-NTA in the plasma membrane and L-ANAP incorporated into three different positions of TRPV1 seems highly unlikely. Furthermore, in various model proteins, the distance dependence and metal dependence of the metal quenching has been shown to be fully accounted for by a FRET mechanism (Latt et al., 1970, 1972; Taraska et al., 2009a,b; Yu et al., 2013). Finally, transition metals decreased the lifetimes of L-ANAP-ME in solution (Fig. 8 D), and bound metals decreased the lifetime of fluorophores attached to a nearby site (Yu et al., 2013). The fraction of the decrease in lifetimes was similar to the fraction of the quenching of steady-state fluorescence, incompatible with static quenching but fully compatible with FRET (Fig. 8 E).

In conclusion, we have presented a new method for measuring the structure and dynamics of membrane proteins relative to the plasma membrane. The application of this method should offer new insights into the molecular dynamics of membrane proteins important for cell signaling.

We thank Dr. Teresa K. Aman and Dr. Abhishek Chatterjee for helpful discussions.

Research reported in this publication was supported by the National Eye Institute of the National Institutes of Health (NIH) under award numbers R01EY017564 (to S.E. Gordon) and R01EY010329 (to W.N. Zagotta), by the National Institute of Mental Health of the NIH under award number R01MH102378 (to W.N. Zagotta), by the National Institute of General Medical Sciences of the NIH under award number R01GM100718 (to S.E. Gordon and W.N. Zagotta), by the National Heart, Lung, and Blood Institute of the NIH under award number T32HL007312 (to E.N. Senning), by the American Heart Association under award number 14IRG18770000 (to W.N. Zagotta), and by the following additional awards from the NIH: S10RR025429, P30DK017047, and P30EY001730.

The authors declare no competing financial interests.

H. Peter Larsson served as guest editor.

Submitted: 14 October 2015
Accepted: 17 December 2015

## REFERENCES

Bjerrum, O.J., and C. Schafer-Nielsen. 1986. Buffer systems and transfer parameters for semidry electroblotting with a horizontal apparatus. *In* Electrophoresis '86: Proceedings of the Fifth Meeting of

the International Electrophoresis Society. M.J. Dunn, editor. Wiley-VCH Verlag GmbH, Weinheim, Germany. 315–327.

Cao, E., M. Liao, Y. Cheng, and D. Julius. 2013. TRPV1 structures in distinct conformations reveal activation mechanisms. *Nature.* 504:113–118. http://dx.doi.org/10.1038/nature12823

Cao, X., L. Ma, F. Yang, K. Wang, and J. Zheng. 2014. Divalent cations potentiate TRPV1 channel by lowering the heat activation threshold. *J. Gen. Physiol.* 143:75–90. http://dx.doi.org/10.1085/jgp.201311025

Caterina, M.J., M.A. Schumacher, M. Tominaga, T.A. Rosen, J.D. Levine, and D. Julius. 1997. The capsaicin receptor: A heat-activated ion channel in the pain pathway. *Nature.* 389:816–824. http://dx.doi.org/10.1038/39807

Caterina, M.J., A. Leffler, A.B. Malmberg, W.J. Martin, J. Trafton, K.R. Petersen-Zeitz, M. Koltzenburg, A.I. Basbaum, and D. Julius. 2000. Impaired nociception and pain sensation in mice lacking the capsaicin receptor. *Science.* 288:306–313. http://dx.doi.org/10.1126/science.288.5464.306

Chatterjee, A., J. Guo, H.S. Lee, and P.G. Schultz. 2013. A genetically encoded fluorescent probe in mammalian cells. *J. Am. Chem. Soc.* 135:12540–12543. http://dx.doi.org/10.1021/ja4059553

Collins, M.D., and S.E. Gordon. 2013. Short-chain phosphoinositide partitioning into plasma membrane models. *Biophys. J.* 105:2485–2494. http://dx.doi.org/10.1016/j.bpj.2013.09.035

De-la-Rosa, V., G.E. Rangel-Yescas, E. Ladrón-de-Guevara, T. Rosenbaum, and L.D. Islas. 2013. Coarse architecture of the transient receptor potential vanilloid 1 (TRPV1) ion channel determined by fluorescence resonance energy transfer. *J. Biol. Chem.* 288:29506–29517. http://dx.doi.org/10.1074/jbc.M113.479618

Förster, T. 1949. Experimentelle und Theoretische Untersuchung des Zwischenmolekularen Ubergangs von Elektronenanregungsenergie. *Z. Naturforsch. A.* 4:321–327.

Fung, B.K., and L. Stryer. 1978. Surface density determination in membranes by fluorescence energy transfer. *Biochemistry.* 17:5241–5248. http://dx.doi.org/10.1021/bi00617a025

Gordon, S.E., E.N. Senning, T.K. Aman, and W.N. Zagotta. 2016. Transition metal ion FRET to measure short-range distances at the intracellular surface of the plasma membrane. *J. Gen Physiol.* http://dx/doi.org/10.1085/jgp.201511530

Heuser, J. 2000. The production of 'cell cortices' for light and electron microscopy. *Traffic.* 1:545–552. http://dx.doi.org/10.1034/j.1600-0854.2000.010704.x

Horrocks, W.D. Jr., B. Holmquist, and B.L. Vallee. 1975. Energy transfer between terbium (III) and cobalt (II) in thermolysin: A new class of metal–metal distance probes. *Proc. Natl. Acad. Sci. USA.* 72:4764–4768. http://dx.doi.org/10.1073/pnas.72.12.4764

Kawate, T., and E. Gouaux. 2006. Fluorescence-detection size-exclusion chromatography for precrystallization screening of integral membrane proteins. *Structure.* 14:673–681. http://dx.doi.org/10.1016/j.str.2006.01.013

Lakowicz, J.R., ed. 2006. Principles of Fluorescence Spectroscopy. Third edition. Springer, New York. 954 pp.

Latt, S.A., D.S. Auld, and B.L. Valee. 1970. Surveyor substrates: Energy-transfer gauges of active center topography during catalysis. *Proc. Natl. Acad. Sci. USA.* 67:1383–1389. http://dx.doi.org/10.1073/pnas.67.3.1383

Latt, S.A., D.S. Auld, and B.L. Vallee. 1972. Distance measurements at the active site of carboxypeptidase A during catalysis. *Biochemistry.* 11:3015–3022. http://dx.doi.org/10.1021/bi00766a013

Lee, H.S., J. Guo, E.A. Lemke, R.D. Dimla, and P.G. Schultz. 2009. Genetic incorporation of a small, environmentally sensitive, fluorescent probe into proteins in *Saccharomyces cerevisiae*. *J. Am. Chem. Soc.* 131:12921–12923. http://dx.doi.org/10.1021/ja904896s

Liao, M., E. Cao, D. Julius, and Y. Cheng. 2013. Structure of the TRPV1 ion channel determined by electron cryo-microscopy. *Nature.* 504:107–112. http://dx.doi.org/10.1038/nature12822

Lishko, P.V., E. Procko, X. Jin, C.B. Phelps, and R. Gaudet. 2007. The ankyrin repeats of TRPV1 bind multiple ligands and modulate channel sensitivity. *Neuron.* 54:905–918. http://dx.doi.org/10.1016/j.neuron.2007.05.027

Loura, L.M. 2012. Simple estimation of Förster resonance energy transfer (FRET) orientation factor distribution in membranes. *Int. J. Mol. Sci.* 13:15252–15270. http://dx.doi.org/10.3390/ijms131115252

Lukacs, V., B. Thyagarajan, P. Varnai, A. Balla, T. Balla, and T. Rohacs. 2007. Dual regulation of TRPV1 by phosphoinositides. *J. Neurosci.* 27:7070–7080. http://dx.doi.org/10.1523/JNEUROSCI.1866-07.2007

Myers, B.R., C.J. Bohlen, and D. Julius. 2008. A yeast genetic screen reveals a critical role for the pore helix domain in TRP channel gating. *Neuron.* 58:362–373. http://dx.doi.org/10.1016/j.neuron.2008.04.012

Nieto-Posadas, A., G. Picazo-Juárez, I. Llorente, A. Jara-Oseguera, S. Morales-Lázaro, D. Escalante-Alcalde, L.D. Islas, and T. Rosenbaum. 2012. Lysophosphatidic acid directly activates TRPV1 through a C-terminal binding site. *Nat. Chem. Biol.* 8:78–85. http://dx.doi.org/10.1038/nchembio.712

Paulsen, C.E., J.P. Armache, Y. Gao, Y. Cheng, and D. Julius. 2015. Structure of the TRPA1 ion channel suggests regulatory mechanisms. *Nature.* 520:511–517. http://dx.doi.org/10.1038/nature14367

Reddy, K.V. 2010. Symmetry and Spectroscopy of Molecules. Second Edition. New Age Science, Tunbridge Wells, England, UK. 631 pp.

Richmond, T.A., T.T. Takahashi, R. Shimkhada, and J. Bernsdorf. 2000. Engineered metal binding sites on green fluorescence protein. *Biochem. Biophys. Res. Commun.* 268:462–465. http://dx.doi.org/10.1006/bbrc.1999.1244

Salazar, H., I. Llorente, A. Jara-Oseguera, R. García-Villegas, M. Munari, S.E. Gordon, L.D. Islas, and T. Rosenbaum. 2008. A single N-terminal cysteine in TRPV1 determines activation by pungent compounds from onion and garlic. *Nat. Neurosci.* 11:255–261. http://dx.doi.org/10.1038/nn2056

Sandtner, W., F. Bezanilla, and A.M. Correa. 2007. In vivo measurement of intramolecular distances using genetically encoded reporters. *Biophys. J.* 93:L45–L47. http://dx.doi.org/10.1529/biophysj.107.119073

Schmied, W.H., S.J. Elsässer, C. Uttamapinant, and J.W. Chin. 2014. Efficient multisite unnatural amino acid incorporation in mammalian cells via optimized pyrrolysyl tRNA synthetase/tRNA expression and engineered eRF1. *J. Am. Chem. Soc.* 136:15577–15583. http://dx.doi.org/10.1021/ja5069728

Schneider, C.A., W.S. Rasband, and K.W. Eliceiri. 2012. NIH Image to ImageJ: 25 years of image analysis. *Nat. Methods.* 9:671–675. http://dx.doi.org/10.1038/nmeth.2089

Smart, D., M.J. Gunthorpe, J.C. Jerman, S. Nasir, J. Gray, A.I. Muir, J.K. Chambers, A.D. Randall, and J.B. Davis. 2000. The endogenous lipid anandamide is a full agonist at the human vanilloid receptor (hVR1). *Br. J. Pharmacol.* 129:227–230. http://dx.doi.org/10.1038/sj.bjp.0703050

Stein, A.T., C.A. Ufret-Vincenty, L. Hua, L.F. Santana, and S.E. Gordon. 2006. Phosphoinositide 3-kinase binds to TRPV1 and mediates NGF-stimulated TRPV1 trafficking to the plasma membrane. *J. Gen. Physiol.* 128:509–522. http://dx.doi.org/10.1085/jgp.200609576

Szolcsányi, J., and E. Pintér. 2013. Transient receptor potential vanilloid 1 as a therapeutic target in analgesia. *Expert Opin. Ther. Targets.* 17:641–657. http://dx.doi.org/10.1517/14728222.2013.772580

Taraska, J.W., and W.N. Zagotta. 2010. Fluorescence applications in molecular neurobiology. *Neuron.* 66:170–189. http://dx.doi.org/10.1016/j.neuron.2010.02.002

Taraska, J.W., M.C. Puljung, N.B. Olivier, G.E. Flynn, and W.N. Zagotta. 2009a. Mapping the structure and conformational movements of proteins with transition metal ion FRET. *Nat. Methods.* 6:532–537. http://dx.doi.org/10.1038/nmeth.1341

Taraska, J.W., M.C. Puljung, and W.N. Zagotta. 2009b. Short-distance probes for protein backbone structure based on energy transfer between bimane and transition metal ions. *Proc. Natl. Acad. Sci. USA.* 106:16227–16232. http://dx.doi.org/10.1073/pnas.0905207106

Tominaga, M., M.J. Caterina, A.B. Malmberg, T.A. Rosen, H. Gilbert, K. Skinner, B.E. Raumann, A.I. Basbaum, and D. Julius. 1998. The cloned capsaicin receptor integrates multiple pain-producing stimuli. *Neuron.* 21:531–543. http://dx.doi.org/10.1016/S0896-6273(00)80564-4

Ufret-Vincenty, C.A., R.M. Klein, M.D. Collins, M.G. Rosasco, G.Q. Martinez, and S.E. Gordon. 2015. Mechanism for phosphoinositide selectivity and activation of TRPV1 ion channels. *J. Gen. Physiol.* 145:431–442. http://dx.doi.org/10.1085/jgp.201511354

Yang, F., L. Ma, X. Cao, K. Wang, and J. Zheng. 2014. Divalent cations activate TRPV1 through promoting conformational change of the extracellular region. *J. Gen. Physiol.* 143:91–103. http://dx.doi.org/10.1085/jgp.201311024

Yao, J., B. Liu, and F. Qin. 2011. Modular thermal sensors in temperature-gated transient receptor potential (TRP) channels. *Proc. Natl. Acad. Sci. USA.* 108:11109–11114. http://dx.doi.org/10.1073/pnas.1105196108

Yu, X., X. Wu, G.A. Bermejo, B.R. Brooks, and J.W. Taraska. 2013. Accurate high-throughput structure mapping and prediction with transition metal ion FRET. *Structure.* 21:9–19. http://dx.doi.org/10.1016/j.str.2012.11.013

Zygmunt, P.M., J. Petersson, D.A. Andersson, H. Chuang, M. Sørgård, V. Di Marzo, D. Julius, and E.D. Högestätt. 1999. Vanilloid receptors on sensory nerves mediate the vasodilator action of anandamide. *Nature.* 400:452–457. http://dx.doi.org/10.1038/22761